

Rational design of acid stable oxide catalysts for OER with OC22

Richard Tran,^{†,‡} Liqiang Huang,^{†,¶} Yuan Zi,[¶] Shengguang Wang,[‡] Benjamin M. Comer,[§] Xuqing Wu,^{||} Stefan J. Raaijman,[§] Nishant K. Sinha,[§] Shibin Thundiyil,[§] Ganesh Iyer,[§] Lars Grabow,^{§,‡} Ligang Lu,[§] and Jiefu Chen[¶]

[†]*Indicates equal contributions*

[‡]*Department of Chemical and Biomolecular Engineering, University of Houston, 4226 Martin Luther King Boulevard, Houston, TX 77204, USA.*

[¶]*Department of Electrical and Computer Engineering, University of Houston, 4226 Martin Luther King Boulevard, Houston, TX 77204, USA.*

[§]*Shell International Exploration and Production Inc., Houston, TX 77082, USA.*

^{||}*Department of Information Science Technology, University of Houston, 14004 University Boulevard #318, Sugar Land, TX 77479, USA.*

E-mail:

Abstract

The efficiency of H₂ production via water electrolysis is typically limited to the sluggish oxygen evolution reaction (OER). As such, significant emphasis has been placed upon improving the rate of OER through the anode catalyst. More recently, the Open Catalyst 2022 (OC22) has provided a large dataset of density functional theory (DFT) calculations for OER intermediates on the surfaces of oxides. When coupled with state-of-the-art graph neural network models, total energy predictions can be achieved with a mean absolute error as low as 0.22 eV. In this work, we interpolated a database of the total energy predictions for all slabs and OER surface intermediates for 4,119 oxide materials in the original OC22 dataset using pre-trained models from the OC22 framework. This database includes all terminations of all facets up to a maximum Miller index of 1 with adsorption configurations for O* and OH*. To demonstrate the full utility of this database, we constructed a flexible screening framework to identify viable candidate anode catalysts under a bulk and nanoscale regime for OER by assessing the price, thermodynamic stability, resistance to corrosion, surface stability, and overpotential. Finally we verified the overpotentials and reaction energies of the final candidate catalysts using DFT. From our assessment, we were able to identify 48 and 69 viable candidates for OER under the bulk and nanoscale regime respectively.

Keywords

Catalysis, oxides, renewable energy, datasets, machine learning, high-throughput screening

Introduction

With the recent congressional passing of the Inflation Reduction Act, there has been an increase in calls for proposals in the field of renewable hydrogen. Electrochemical water splitting, or water electrolysis, is a sustainable and promising means of producing H_2 thanks to the wide abundance of water. This process involves two coupled half-reactions: hydrogen evolution reaction (HER) and the significantly slower oxygen evolution reaction (OER) which has primarily been the bottleneck in advancing water-splitting technology. The search for a highly active anode catalyst for OER is therefore paramount to the realization of practical water splitting technology.¹⁻⁴

Transition metal oxides are a promising class of catalysts for OER due to their varying oxidation states for more efficient multi-electron transfer, stability under highly acidic conditions favorable towards OER, and active undercoordinated transition metals sites. In regards to commercialized catalysts, IrO_2 and RuO_2 are the benchmark catalysts for OER, exhibiting low overpotentials (an indicator of activity) of 0.25 to 0.5 V under acidic conditions.⁵ However, the material cost of precious metals (\$18,315.36 and \$155,727.85 per kg for RuO_2 and IrO_2 respectively) limits their widespread adoption. Consequently, there is much desire to identify cheaper materials for catalysts in OER while maintaining similar performance.

Despite the abundance of unary and binary oxides, very few are capable of exhibiting both high catalytic activity and stability under operating conditions. Computational analysis performed by Wang et al.⁶ indicated only 68 bimetallic oxides from a pool of 47,814 were stable with a Pourbaix decomposition energy (ΔG_{PBX}) of 0.5 eV/atom or less under acidic conditions (pH=0) and an applied potential cycle between 1.2 and 2.0 V. Gunasooriya and Nørskov⁷ calculated the overpotential of these candidate oxides and identified only 10 non-binary metal oxides with a promising overpotential of less than 0.8 V.

It is possible that many materials filtered out by the highly discriminant electrochemical sta-

bility criteria can also exhibit competitive overpotentials if stabilized. Nanoscale stability, elemental doping, and the introduction of oxygen vacancies have been demonstrated to be effective means of improving stability.^{1,8,9} Nanoscaling in particular presents a promising avenue for stabilizing oxides under operating conditions while exposing a greater number of active sites through the increasing surface area-to-volume ratio (SA:V).¹⁰⁻¹²

However, an accurate evaluation of the nanoparticle formation energy not only requires the thermodynamic contributions of the bulk, but the surface as well. Doing so requires an ensemble of expensive Density Functional Theory (DFT) calculations of the bare surfaces for one material. Likewise, accurate evaluations of the overpotential requires an even larger set of calculations for all the surface intermediates participating in OER. As such, doing so for the massive pool of binary and unary oxide materials available will quickly become computationally expensive and unfeasible.

Machine learning (ML) potentials and screening frameworks have recently contributed significantly in rapidly predicting candidate catalysts without the need for expensive systematic DFT screening.¹³⁻¹⁷ Among these efforts, the Open Catalyst Project (OCP)¹⁸ framework has stood out as having the largest dataset of carefully curated DFT calculations for non-oxide slabs and surface intermediates to-date. ML models pre-trained with the OCP has allowed for large scale interpolation efforts to predict binding energies, enabling in high-throughput screening efforts to identify viable catalyst candidates¹⁹ and explore fundamental surface chemistry.²⁰ More recently, the Open Catalyst 2022 (OC22) framework has expanded upon this dataset by incorporating random combinations of 4,728 oxide materials, Miller indices up to 3, and surface intermediates involved in OER.²¹ These efforts have yielded predictive ML models with total energy mean absolute error (MAE)s of up to 0.22 and 0.69 eV for *in domain* (materials observed during training) and *out of domain* predictions respectively.

In this manuscript, we utilized a pre-trained model from the OC22 framework to interpo-

late the surface energies and OER binding energies for all 4,119 *in domain* oxide materials on all facets up to a maximum Miller index of 1. To demonstrate the applicability of our interpolated database, we constructed a high-throughput screening framework with a set of progressive criteria that can be modified or expanded upon for ease of customizeability in order to evaluate the commercial and practical viability of each material for OER. Our general framework evaluates materials based on thermodynamic stability, overpotential, and material cost. We also expand upon other screening criteria such as the possibility of nanoscale stabilization or the faceting of surfaces on the equilibrium crystal structure. We propose 48 and 69 possible candidates for OER under the bulk and nanoscale regime respectively that warrant further experimental investigation.

Methods

All analysis were performed using the python materials genomics (*pymatgen*)²²⁻²⁵ and Atomic Simulation Environment (ASE)²⁶ packages.

Slab generation

We described all surfaces considered in this work with a slab model containing an atomic and vacuum layer of 12.5 Å thick. We explored all facets up to a maximum Miller index of 1 for all 4,119 oxide materials considered in OC22. The bulk materials used for slab construction in this study were obtained from the Materials Project.²⁷ We also considered all terminations for each facet (*sans* slabs exceeding 200 atoms) while maintaining equivalent surfaces on both sides of the slab which consequently resulted in non-stoichiometric slabs with respect to the bulk formula. For all slabs constructed, we modelled the surface intermediates of O* and OH*. To avoid periodic interactions between the adsorbates, all slabs were expanded along the length and width to at least 8 Å. We assumed all adsorbates bind through the O atom on available undercoordinated metal sites. All

bare surface and surface intermediate models were constructed using the python framework adapted from OC22.^{21,28,29}

DFT and machine learning settings

All DFT calculations were performed using the Vienna *Ab Initio* Simulation Package (VASP)³⁰⁻³³ within the Projected Augmented Wave (PAW)³⁴ approach. We modeled the exchange-correlation effects with the Perdew-Berke-Ernzerhof (PBE) generalized gradient approximation (GGA) functional.³⁵ All calculations were performed with spin-polarization with a plane wave energy cut-off of 500 eV. The energies and atomic forces of all calculations were converged to within 1×10^{-4} eV and 0.05 eV Å⁻¹, respectively. We used Γ -centered k-point meshes of $\frac{30}{a} \times \frac{30}{b} \times 1$ for slab calculations, with non-integer values rounded up to the nearest integer. We also apply a Hubbard U correction to chemical systems as suggested by the Materials Project³⁶ to account for missing electron interactions.

We used a pre-trained model for the ***Structure to Energy and Forces*** (S2EF)-*Total* task from the OC22 framework to perform all machine learning predictions of the relaxed structure and total energy. The entirety of the Open Catalyst 2020 (OC20) dataset (1,281,040 DFT relaxations) was used to train an S2EF-*Total* model which was subsequently fine-tuned with the OC22 dataset (62,331 DFT relaxations) to better predict the total energies of oxide surfaces and surface intermediates. The model was trained using the GemNet-OC architecture³⁷ due to its superior performance in energy predictions when compared to other graph neural network (GNN) architectures as a consequence of its improved capturing of long-range and quadruplet interactions.

For further details regarding additional parameters used in VASP or the construction of the machine learning model, we refer the reader to Tran et al.²¹.

All OC22 S2EF predictions and DFT calculations of slabs were performed with selective dynamics. In regards to surface energy predic-

tions, both the bottom most and topmost layer of atoms within 1.25 Å were allowed to relax in the bare slab in order to ensure both surfaces had equal surface energy contributions. For the adsorption energies, only the topmost layer of atoms within 1.25 Å and any adsorbates were allowed to relax in the bare slab and surface intermediates. To avoid inadvertent desorption and dissociation of adsorbates during our ML relaxation, we applied a spring constant of 7.5 eV Å⁻² between all adsorbate atoms to preserve the identity of the molecule and between the adsorbate and host surface atoms whenever the adsorbate drifts 2 Å away from its initial position along the axis perpendicular to the surface.^{38,39} Similarly, we also applied the same restorative force to all surface atoms when the relaxed trajectory exceeds 1 Å from the initial position of the ions to avoid drastic surface reconstruction.

Surface thermodynamics

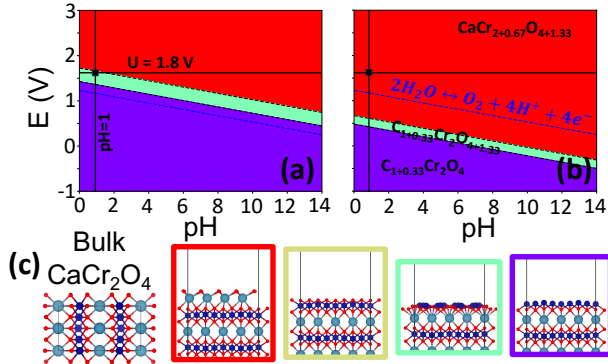


Figure 1: Surface Pourbaix diagram of the (001) facet of CaCr_2O_4 at $T = 80^\circ\text{C}$ under $\Delta\mu_{\text{Cr}} = -4$ eV (a) and $\Delta\mu_{\text{Cr}} = 0$ eV (b). The blue dashed line indicates the equilibrium conditions for OER while the black box indicates the desired conditions for OER ($p\text{H} = 1$ and $U = 1.8$ V). The phases in (a) and (b) are color coded with the corresponding terminations of the (001) facet in (c).

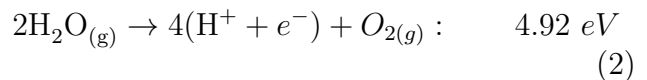
All bare slabs of formula $\text{A}_{\text{nx}}\text{B}_{\text{ny}+\text{k}}\text{O}_{\text{nz}+\text{j}}$, with A and B being two metal components, are constructed from a bulk ternary oxide of $\text{A}_x\text{B}_y\text{O}_z$. We can calculate the surface energy of any slab

of $\text{A}_{\text{nx}}\text{B}_{\text{ny}+\text{k}}\text{O}_{\text{nz}+\text{j}}$ with the following:

$$\gamma(\mu_{\text{B}}, \mu_{\text{O}_2}) = \frac{E_{\text{slab}}^{\text{A}_{\text{nx}}\text{B}_{\text{ny}+\text{k}}\text{O}_{\text{nz}+\text{j}}} - (nE_{\text{bulk}}^{\text{A}_x\text{B}_y\text{O}_z} + k\mu_{\text{B}} + j\frac{1}{2}\mu_{\text{O}_2})}{2A} \quad (1)$$

where $E_{\text{slab}}^{\text{A}_{\text{nx}}\text{B}_{\text{ny}+\text{k}}\text{O}_{\text{nz}+\text{j}}}$ is the total energy of the bare slab, $E_{\text{bulk}}^{\text{A}_x\text{B}_y\text{O}_z}$ is the total energy per formula unit of the bulk crystal, and A is the surface area. The chemical potentials, μ_i , accounts for any nonstoichiometric species (with respect to bulk stoichiometry) in the slab formula.

The chemical potential of oxygen ($\Delta\mu_{\text{O}_2}$) can be referenced to the electrochemical decomposition of water to $\text{O}_{2(\text{g})}$:



which allows us to rewrite μ_{O_2} (and thereby γ) as a function of $p\text{H}$ and applied potential (U) as such:

$$\Delta\mu_{\text{O}_2} = 4.92 + 2\mu_{\text{H}_2\text{O}}^0 - 4\left(\frac{1}{2}\mu_{\text{H}_2}^0 - eU - k_{\text{B}}T p\text{H} \ln 10\right) + \Delta G_{\text{corr}}^{*\text{O}} \quad (3)$$

where $\Delta G_{\text{corr}}^{*\text{O}}$ corrects for the Gibbs free energy of excess or deficient oxygen at the surface (see Tran et al.²¹ and Gunasooriya and Nørskov⁷ for details). We will assume optimal operating conditions for OER ($p\text{H} = 1$ and $U = 1.8$ V at $T = 80^\circ\text{C}$)^{6,40} ($\Delta\mu_{\text{O}_2} = -1.30$ eV) when assessing the bulk formation energy and surface energy of all materials as illustrated in Figure 1(a-b). For slabs containing excess or deficient metal (B) species, the chemical potential of component B is conventionally referenced with respect to the per atom energy of the ground state bulk crystal of pure component B (e.g. $\mu_{\text{Fe}} = \Delta\mu_{\text{Fe}} + E_{\text{BCC,Fe}}^{\text{DFT}}$). By varying the chemical potential of component B, we can stabilize different surface terminations of the same facet as shown in the surface Pourbaix diagram in Figure 1(a-b).

To determine the nanoscale stability of metastable and unstable materials under operating conditions, we assessed the nanoparticle formation energy given by:

$$G_f^{NP} = E_V(pH, V, T) \left(\frac{4}{3} \pi r^3 \right) + \bar{\gamma}(pH, V, T, \Delta\mu_M) (4\pi r^2) \quad (4)$$

whereby E_V is the Pourbaix formation energy per volume of the unit cell, $\bar{\gamma}$ is the weighted surface energy of the Wulff shape (an analogue to the nanoparticle morphology), and r is the radius of the nanoparticle. Detailed explanation of these quantities can be found in the Supplementary Information. Figure 2 demonstrates how a less stable compound (CaTi_2O_5) can become more stable than the ground state compound as nanoparticle size and $\Delta\mu_{\text{Ti}}$ decreases. The size effect will change the relative contribution of surface energy and bulk Pourbaix formation energy to G_f^{NP} while $\Delta\mu_{\text{Ti}}$ changes the overall particle morphology and thereby surface energy of the particle.

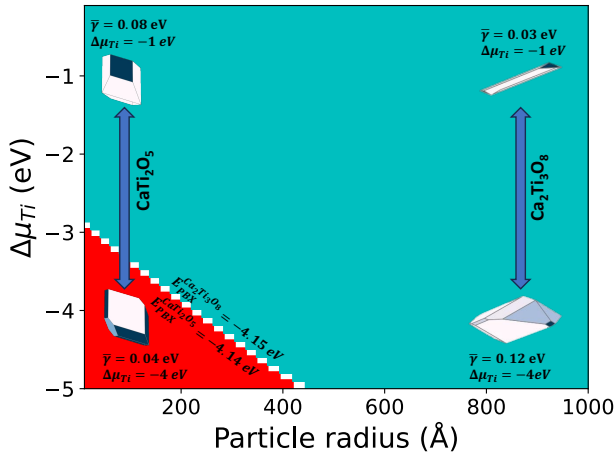


Figure 2: Nanoscale stability phase diagram for the Ca-Ti-O chemical system plotted using G_f^{NP} as a function of the chemical potential of Ti ($\Delta\mu_{\text{Ti}}$) and nanoparticle radius. The red region represents the less stable (higher E_{PBX}) phase (CaTi_2O_5) while the cyan region represents the ground state phase ($\text{Ca}_2\text{Ti}_3\text{O}_8$). The nanoparticle morphology and surface energy change as a function of $\Delta\mu_{\text{Ti}}$ indicated by the inset Wulff shapes.

The scope of this study will explore the water nucleophilic attack (WNA) mechanism for OER, a four step mechanism where two water molecules sequentially bind to a metal at the surface and release an electron-proton pair at

each step as shown in Figure 3. We can determine the overpotential for this reaction by identifying the largest energy difference between each step (reaction energy) with the following:

$$\eta = \max(\Delta G^i, \Delta G^{ii} - \Delta G^i, \Delta G^{iii} - \Delta G^{ii}, 4.92 - \Delta G^{iii}) / e - 1 \quad (5)$$

where ΔG^i , ΔG^{ii} , and ΔG^{iii} are the Gibbs free energy of each reaction step, 4.92 eV is the Gibbs free energy to dissociate two water molecules into O_2 and $4(\text{H}^+ + \text{e}^-)$ shown in Equation 2, and 1.23 V is the equilibrium potential for water decomposition. We can derive the Gibbs free energy of each step listed in Equations $i - iv$ (see Figure 3) as such:

$$\Delta G^i = E_{ads}^{\text{OH}^*} + \Delta G_{corr}^{\text{OH}^*} + \mu_{\text{H}^+} + \mu_{\text{e}^-} \quad (6)$$

$$\Delta G^{ii} = E^{\text{O}^*} + \Delta G_{corr}^{\text{O}^*} + 2(\mu_{\text{H}^+} + \mu_{\text{e}^-}) \quad (7)$$

$$\Delta G^{iii} = E^{\text{OOH}^*} + \Delta G_{corr}^{\text{OOH}^*} + 3(\mu_{\text{H}^+} + \mu_{\text{e}^-}) \quad (8)$$

where $E_{ads}^{\text{OH}^*}$, $E_{ads}^{\text{O}^*}$, and $E_{ads}^{\text{OOH}^*}$ are the electronic adsorption energies of the intermediates for OER and $G_{corr}^{\text{OH}^*}$, $G_{corr}^{\text{O}^*}$, and $G_{corr}^{\text{OOH}^*}$ are correction terms for the Gibbs free energy derived in the Supplementary Information of OC22.²¹

Alternatively, if E^{OOH^*} is unavailable, well known scaling relationships between ΔG^{iii} and ΔG^i can be used instead:^{7,21}

$$\Delta G^{iii} = \Delta G^i + 3.26 \quad (9)$$

Due to the significantly larger degrees of rotational freedom in OOH^* which increases the complexity of possible adsorbate placements, we will omit ML predictions of OOH^* intermediates and estimate ΔG^{iii} from Equation 9.

Only the most stable site for OH^* dictated by $E_{ads}^{\text{OH}^*}$ from a set of considered adsorption sites on the same surface is considered when determining η . We maintain the adsorption site corresponding to the most stable site of OH^* when considering $E_{ads}^{\text{O}^*}$.

Further details regarding the derivation of all thermodynamic quantities and scaling relationships can be found in the Supplementary Information.

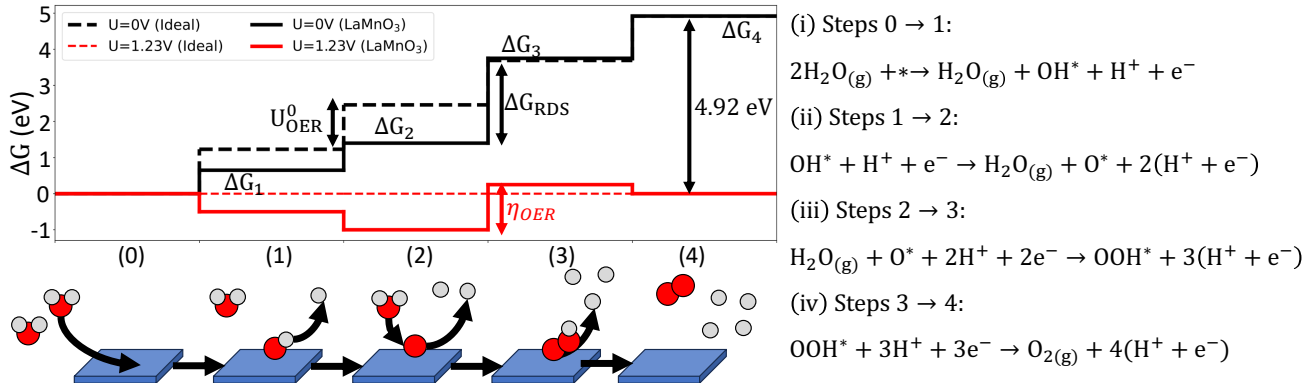


Figure 3: Reaction diagram for the WNA on an ideal catalyst (dashed lines) and LaMnO_3 (100) surface (solid lines) at 0 V (black) and the equilibrium potential of OER (red). An illustration of each reaction step is shown at the bottom (red circles are oxygen while grey circles are hydrogen/protons). Reaction energies for LaMnO_3 were derived from Man et al.⁴¹. The chemical equation between each reaction step (1-4) is listed on the right (*i-iv*).

Results and Discussion

Database scope and usage

We emphasize that the purpose of both the OC20 and OC22 datasets was to establish a large and diverse set of DFT calculated surfaces and surface intermediates for the purpose of training ML potentials generalized to infer the total DFT of any slab and adsorbate combination. To maximize the diversity of the sample set, the OCP curated DFT calculations of randomly selected combinations of materials, surfaces, and adsorbates. The scope of the dataset **does not** encompass a comprehensive database for evaluating η directly, as many necessary datapoints are missing illustrated in Figure 4. The construction of a comprehensive database is a herculean task that is immeasurably costly and time consuming with DFT alone. However, by consolidating the S2EF-*total* model to predict thermodynamic overpotentials, we can potentially infer the catalytic activity of large material datasets for OER within a reasonable degree of error with respect to DFT.

Using the previously developed ML models, we systematically extrapolated the total DFT energy of all terminations for all facets up to a maximum Miller index of 1 for all 4,119 materials considered in this study. We then extrapolated the total energy of all metal adsorp-

tion sites on all surfaces for O^* and OH^* . Table 1 summarizes the scope of our extrapolated database. In contrast to our interpolation efforts, the size of the OC22 dataset for O^* and OH^* is only 0.1% of the the predicted dataset in this work. Despite requiring orders of magnitude less computational resources than a DFT dataset of the same size, the estimated cost to produce our dataset is still 9,473.9 GPU-hrs. (an average rate of one prediction every 12.5 seconds), a significant amount of resources. By making this database freely available to the scientific community, users interested in performing similar high-throughput screening exercise or fundamental analysis can do so without the enormous cost in GPUs. The entire database including the initial and relaxed structures and total energies can be accessed through the University of Houston Dataverse Repository.⁴² Details regarding the database metadata are given in the Supplementary Information.

Table 1: Summary of database scope

# predictions: 2,728,470	
# materials: 4,119	
# slab predictions: 183,560	
Ave. # slabs per material: 46	
# adsorbed slab predictions: 2,544,910	
OH^*	O^*
1,901,804	643,106

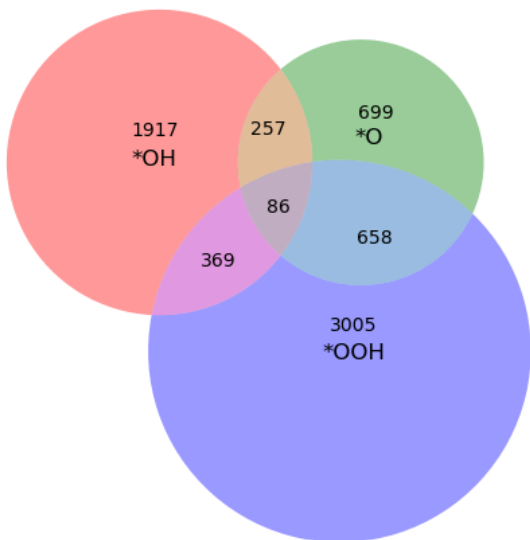


Figure 4: Scope of surface intermediates for OER calculated using DFT in the OC22 dataset. Overlaps indicate the number of surfaces where different intermediates (OH^* , O^* , or OOH^*) are calculated for the same surface.

Validating machine learning with DFT

We used DFT to validate 68 values for the reaction energies corresponding to Equations *i-iii* for 30 Pourbaix stable compounds in our database. The R^2 of the test set shown in Figure 5(a) is 0.91, indicating strong linear correlation between the DFT and ML quantities. The MAE is 0.382 eV, which is slightly larger than the MAE of 0.239 eV obtained from the validation set in the original OC22 assessment.²¹ All materials sampled in the test set were in-domain of the training and validation sets, however, the facets, terminations and adsorbate configurations reflect a comprehensive assessment that was not considered on the original OC22 dataset. The strong linear correlation and consistent MAE with this test set indicates that our model is generalized for any surface and adsorbate configuration on the material set found in OC22.

Next we assess the predictability of the ML inferred overpotential (Equation 5) using the predicted and calculated values of reaction energy

from Figure 5(a). Figure 5(b) once again plots the DFT calculated data points against the corresponding ML quantities. The R^2 of the test set is 0.742, indicating strong linear correlation between the DFT and ML quantities while the MAE is 0.205 eV. Our predictions successfully determined the overpotentials of the two well-accepted benchmark catalysts for OER: IrO_2 and RuO_2 . Furthermore, DFT calculated overpotentials less than 0.75 eV are also consistent with our ML predictions, demonstrating that our predictions are capable of identifying active catalysts.

High-throughput screening

Figure 6 summarizes the selection criteria that we employed to screen for candidate electrocatalysts for OER. The first criteria in our high-throughput screening framework was to determine if a material exists in the original training dataset of OC22. As previously demonstrated by Tran et al.²¹, the OC22 framework is capable of predicting the total DFT energies of slabs and surface intermediates of oxides within a mean absolute error of 0.22 eV for materials that have been observed in the training dataset. This includes 4,732 unique crystal structures obtained from the Materials Project with 318 unary oxides (A-O) and 4,414 binary oxides (A-B-O). Our database will only interpolate the energies of slabs and surface intermediates amongst these materials (for more information, the reader is redirected to²¹).

The second criteria describes the Pourbaix stability, i.e., the electrochemical stability of a material in an aqueous environment. Here, we can interpret Pourbaix stability under a bulk regime (right side of Figure 6). We quantify the Pourbaix stability of the bulk using the Pourbaix decomposition energy (E_{PBX}), which is a function of the temperature (T) applied potential (U) and pH of the environment (at $T = 80^\circ\text{C}$, $U = 1.8 \text{ V}$, and $\text{pH} = 1$). Materials with $E_{PBX} = 0 \text{ eV atom}^{-1}$ are stable under such conditions while materials with $E_{PBX} < 0 \text{ eV atom}^{-1}$ are metastable with the likelihood of corrosion increasing with E_{PBX} . It was shown experimentally that metastable ma-

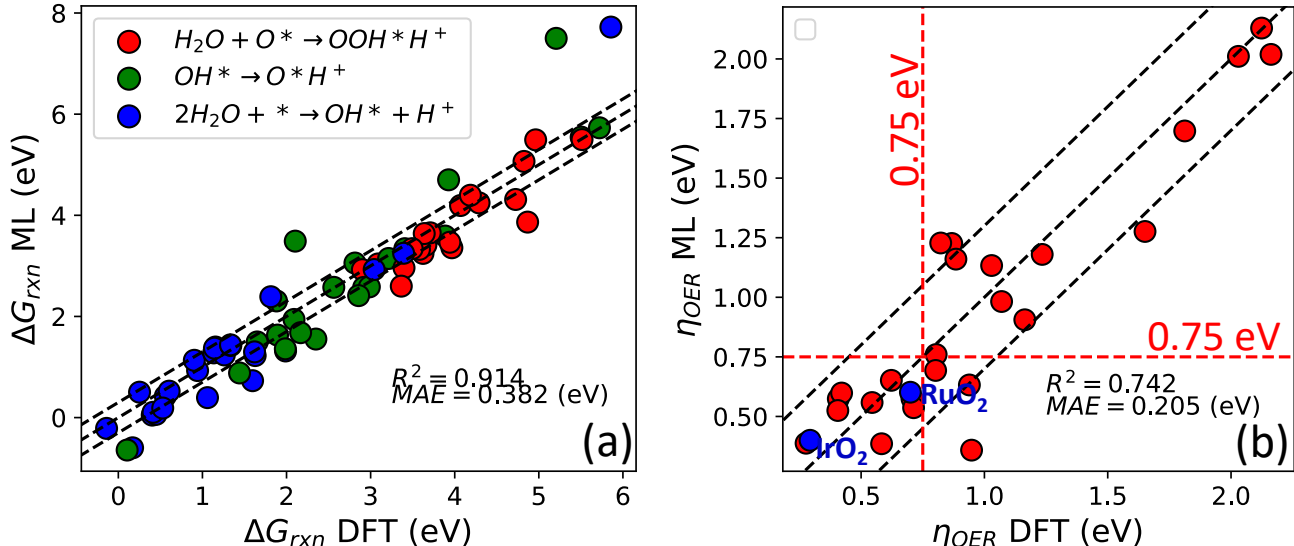


Figure 5: (a) DFT calculated data points for reaction energy plotted against the corresponding ML predicted quantities. (b) DFT calculated data points for overpotential plotted against the corresponding ML predicted quantities. Overpotentials of the benchmark materials are highlighted in blue (IrO_2 and RuO_2). Overpotentials of less than 0.75 eV are considered catalytically active.

materials with $E_{PBX} \leq 0.2$ eV atom $^{-1}$ are less likely to dissolve or corrode.⁴³ However, materials with E_{PBX} as high as 0.5 eV atom $^{-1}$ have also been shown to be stable, albeit with a degree of surface passivation which can inhibit catalytic activity.²⁴ We allow any material with $E_{PBX} \leq 0.5$ eV atom $^{-1}$ under the aforementioned conditions (see Figure 1)(a) to satisfy this criterion. Due to the exclusive nature of E_{PBX} , only 1,853 of the original 4,119 materials will satisfy this criterion.

In our third criteria, we assess the surface energy of every termination for each facet of each material that is Pourbaix stable with Equation 1. From the surface energy, we were able to construct the Wulff shape which indicates the most prominent facets in an equilibrium crystal. When considering which surfaces are stable and can potentially facilitate OER, we only consider surfaces that appear on the Wulff shape. Depending on the stoichiometry of the slab, the surface energy can vary as a function of $\Delta\mu_M$. For simplicity, we will roughly assume a possible chemical potential range of the metal M as $-5 < \Delta\mu_M < 0$ eV when interpreting surface energy. Wulff shapes containing negative surface energies are ignored as nonphysical so-

lutions as this indicates the surface is more stable than the bulk (which implies dissolution of the solid). The dissolution of the Wulff shape will consequently lead to 343 additional materials being omitted from our list of candidates, leaving us with 1,552 materials with 6,210 stable surfaces on the Wulff shape.

In our fourth criteria, we assess the overpotential of each candidate surface with Equation 5. We consider any material at least two facets on the Wulff shape exhibiting $\eta < 0.75$ V as being potentially competitive with RuO_2 and IrO_2 in regards to catalytic efficiency. We find that 61 materials (343 surfaces) from our previous 1,552 materials will satisfy this criteria.

The fifth criteria assesses the thermodynamic stability of the candidate material via the energy above hull (E_{hull}) or the formation energy of a material relative to the ground state. Like with Pourbaix stability, materials with a calculated $E_{hull} > 0$ eV atom $^{-1}$ are metastable with the likelihood of experimental synthesizability decreasing as E_{hull} increases. Materials with a calculated $E_{hull} \leq 0.1$ eV atom $^{-1}$ have been shown to have reasonable rates of demonstrated synthesis in experiment.⁴⁴ From our aforementioned 61 catalytically active candidates, we

identify 55 materials that are metastable.

The final criteria assesses the material cost of each compound in \$/kg/mol. To satisfy this criteria, the cost of a compound must be less than that of RuO₂ or \$18,315/kg/mol (as of March 2021⁴⁵⁻⁴⁷). We have identified 48 materials from our 55 metastable materials that have satisfied this criteria.

Lastly, we use DFT to assess the lowest overpotential for a sample set of seven candidate materials. We observe that the overpotentials determined from both DFT and ML are less than 0.75 eV, our threshold for catalytic efficiency. Details in regards to all proposed candidates can be found in the Supplementary Information.

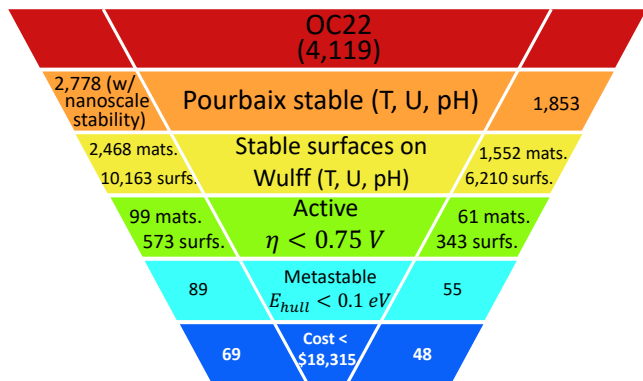


Figure 6: Summary of the screening criteria considered in our high-throughput screening framework. The possible number of candidates that have satisfied each tier is listed on the right for bulk Pourbaix stable materials and on the left when nanoscale stability is possible. The second and third criteria can be further modified by changing the environmental parameters (T, U, pH).

Of the candidate materials exhibiting low overpotential for two or more facets, Co, Co-Ni, Ca-Fe, Fe-Co, and Zn-Co oxides have all been reported in the experimental literature. We also report candidates containing Pb, Cr, and Cd however, these components are known to possess potential health risks⁴⁸ and as such, caution is advised for any further investigation of candidates containing these elements. As far as we are aware, the other 34 bulk stable, non-toxic materials identified through this screening

framework have yet to be explored in the literature. The discovery of a potential candidate for OER demonstrates the potential of ML-assisted screening techniques in identifying novel catalysts.

Overpotential assessment

Figure 7(a) shows the 36 elements on the periodic table considered in our database. The heatmap indicates the number of materials containing an element that exhibits at least 2 facets with $\eta < 0.75 V$. Oxide combinations containing Co, Ag, Ni, Cu, and arguably Mn tend to form catalysts that exhibit low overpotentials. Ag-based chemical systems such as Ag-O,⁵¹ Ag-Bi-O,⁵² Ag-Cu-O,⁵³ and Ag-Co-O⁵⁴ have been demonstrated as viable catalysts for OER in experimental settings. The common use of Ag has been attributed to the fact that Ag has the highest electrical conductivity amongst all metals, allowing it to easily facilitate the four electron charge transfer process that takes place during OER.⁵⁴ Although it is not as common and cheap as the 3d transition metals, Ag is still more reasonably priced than the other noble metals. Furthermore, it has been shown that Ag-doping at 1% has been enough to enhance charge transfer in OER,⁵⁵ making Ag-based oxides reasonably economical. Similarly, Mn-based chemical systems are also known to be promising catalysts for OER. This is owed to the intrinsically high activity and number of polymorphs for compounds of MnO_x⁵⁶ which can be synergistically improved when introducing other components such as Fe,⁵⁷ Ni,⁵⁸ and Co⁵⁹

Non-noble chemical systems such as Cu-Zn, Co-Fe, Fe-Ni, Cu-Ni, Co-La, Co-Ti, Fe-Mn, Cu-Fe, La-Ni, La-Mn, La-Sr, Ba-Ni, Fe-Sr, Fe-La, Fe-Fe, Mn-Mn, Co-Mn, Co-Cr, and Co-V-based oxides have been shown to exhibit competitive overpotentials in the experimental literature (see references herein^{2-4,49,50}) despite their absence from our final set of candidates. To account for this discrepancy, we predicted the overpotentials for all Wulff shape facets of all 4,119 materials. We summarized the overpotential of each chemical system by plotting the

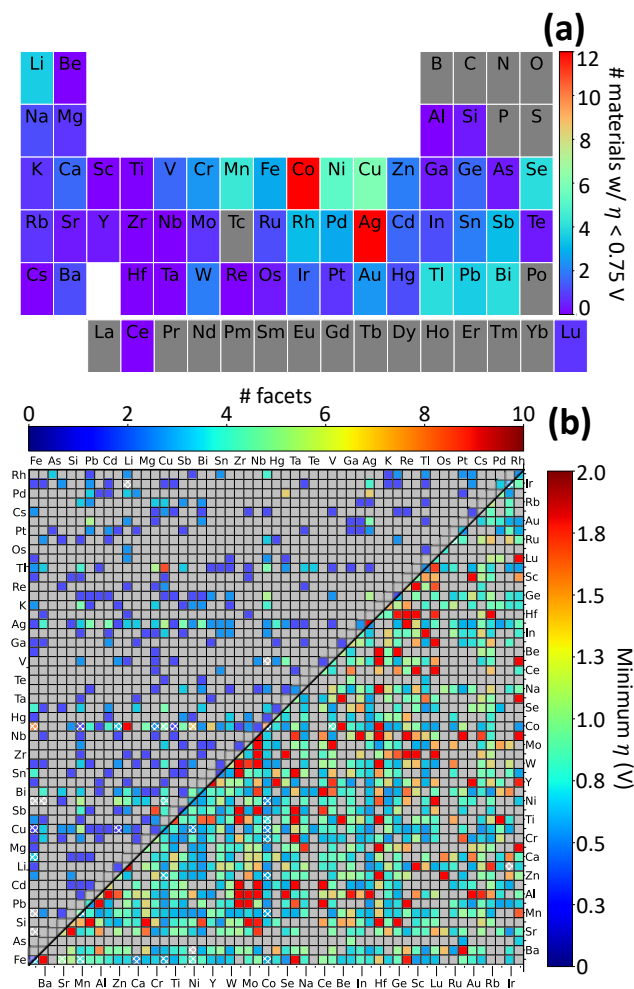


Figure 7: (a) Periodic table of elements considered in the database. Colormap indicates the number of materials containing the element that exhibit $\eta < 0.75$ V for at least two facets. (b) Grid map for each pair of elements with colors indicating the lowest overpotential amongst all facets on the Wulff shape containing this chemical system (bottom right) and the number of facets on the Wulff shape across materials with the same chemical system that exhibit overpotentials less than 0.75 eV (top left). Tick labels on the x- and y-axis are sorted from the cheapest (Fe) to the most expensive (Rh) element. Grids containing white hatches correspond to chemical systems that exhibit $\eta < 0.75$ V in the experimental literature (see references herein^{2-4,49,50}).

lowest overpotential and the number of facets exhibiting $\eta < 0.75$ eV in Figure 7(b) across

all materials of the same chemical system as a heat map. Upon further inspection, Fe-Mn-O, Cu-Ni-O, Ba-Ni-O, and Mn-O are shown to be relatively unstable in our dataset ($E_{hull} > 0.1$ eV or $E_{Pbx} > 0.5$ eV) despite having competitive overpotentials corroborating with past experiments. Fe-Mn-O, Ba-Ni-O, and Mn-O can be relatively stable under less acidic conditions on the Pourbaix diagrams, however corrosion will begin to occur under highly acidic (pH=1) conditions resulting in $E_{Pbx} > 0.5$ eV. Meanwhile Cu-Ni-O corresponds to a spinel structure which can destabilize under redox processes.⁶⁰

We have demonstrated 360 chemical systems exhibiting facets on the Wulff shape that are potentially active for OER despite only 48 chemical systems (ignoring material cost) appearing in our set of candidates due to the the bulk stability of many materials being inaccessible. Methods for stabilizing bulk oxides such as nanoscale stability, elemental doping, and the introduction of oxygen vacancies have been demonstrated to be effective means of improving stability.¹ RuO₂ for example is known to have stability issues in aqueous environments despite being the benchmark for OER catalysts. However doping with other metals such as Cr and Ti has been shown to stabilize this material.⁸ With these methods of stabilizing the catalyst material and accessing active surfaces, we emphasize that the identification of viable catalysts should not strictly be confined by the Pourbaix stability or even E_{hull} . As an example, we will demonstrate how nanoscale stabilization can potentially expand the material space available for OER to access these materials.

Alternative screening frameworks

In this study we constructed a database of machine learning data and demonstrated how it can be used in a variety of ways to screen for catalyst. First, we identified potential candidates for OER by creating a screening framework based on simple bulk thermodynamic (the energy above hull and Pourbaix energy above hull) and surface stability arguments. We will now modify our framework by introducing an

additional layer of complexity to our definition of Pourbaix stability by analyzing the possibility of nanoscale stability under acidic conditions for OER as shown in Figure 6 (right). Using our nanoscale stability diagrams (see Figure 2), we were able to identify 2,778 Pourbaix stable materials with 886 stabilizing at the nanoscale regime (10 to 100 nm). From our Wulff shape analysis of the 2,778 Pourbaix stable materials, we identified 10,163 surfaces that appear on the Wulff of 2,468 materials. We find that 573 of these surfaces (from 99 materials) also exhibit low overpotentials. From these 99 potentially active materials, 89 are metastable and 69 exhibit a material cost less than RuO_2 . In total we have identified 17 additional candidates that are potentially commercially viable for OER if these materials can be synthesized as nanoparticles.

Another example of how we can modify our screening framework is by changing our criteria for surface stability. As mentioned before, we only considered facets that appear on the Wulff shape within a metal chemical potential between $-5 < \Delta\mu_M < 0\text{eV}$. The Wulff shape indicates the most statistically likely facets to appear under equilibrium crystal growth conditions. However, non-equilibrium conditions can potentially force different types of facets to appear.⁶¹ We can account for this in our screening framework by considering all facets as viable surfaces for OER. With this simple assumption, we identified 98 materials (72 and 26 in the bulk and nanoscale regime respectively) with $E_{PBX} < 0.5\text{ eV}$, $\eta < 0.75\text{ V}$ (for more than one facet), $E_{hull} < 0.1\text{ eV}$, and with a material cost less than RuO_2 (see Table 3-5 in the Supplementary Information).

Other alternative screening frameworks can be explored by simply adding or modifying existing criteria. As a simple example, we can assess Pourbaix stability under different temperature conditions. The operating temperatures for OER are typically between 60°C and 80°C with higher temperatures resulting in improved ionic conductivity and kinetics in exchange for lower stability. Although our assessment assumes an operating temperature of 80°C , we can easily re-assess the second criteria (for bulk

stability) in our screening framework at 60°C instead which will stabilize two additional final candidates: $\text{Cr}(\text{SbO}_3)_2$ and FeSnO_3 .

We can also redefine our definition of Pourbaix stability by only considering materials that are stable within an applied potential range of $1.2 < U < 2\text{ V}$ which will significantly reduce the number of possible candidates as shown by Wang et al.⁶ We can even explore alternative possible reaction mechanism by exploring the potential of oxides for as dynamic catalysts through pH-switching.⁶² We can do so by changing the surface environment on a facet to optimize different reaction steps. This can lead to a dynamic reduction in overpotential that cannot be accessed through static catalysis alone. We hope to demonstrate the ease and variability of how these frameworks can be modified to illustrate the utility of these machine learning databases. We highly encourage the scientific community to use our database to explore such possibilities in the future.

Conclusions

In this contribution, we employed pre-trained machine learning potentials from the Open Catalyst Project to develop a publicly available database of O^* and OH^* surface intermediates for 4,119 oxide materials. We demonstrated the utility and variability of this database by presenting several easily implemented high-throughput screening frameworks for identifying thermodynamically stable and catalytically active (low overpotential) materials for oxygen evolution reaction from our initial pool of 4,119 candidates. Our first screening framework identified 48 candidates that are Pourbaix stable in the bulk regime with catalytic surfaces that appear on the Wulff shape. By slightly modifying this framework to account for the possibility of nanoscale stability, we identified 17 additional candidates. A more simplified (but less robust) framework identified 74 candidates in total by considering Pourbaix stable materials in the bulk regime without requiring facets to appear on the Wulff shape. When ignoring material cost and bulk stability, we find that

oxides containing Co, Cu, Ni, Ag, and Mn tend to exhibit overpotentials that are potentially competitive with current benchmark materials (IrO₂ and RuO₂). We plan to further expand our database to include other potential reaction mechanisms for OER such as the oxo-coupling mechanism and lattice oxygen evolution. We hope this database will encourage future investigators to develop their own high-throughput screening frameworks.

Author Contributions

Richard Tran implemented the screening framework and performed DFT calculations. Liqiang Huang designed the parameters and software to manage and automate predictions and performed ML predictions. Yuan Zi, Shengguang Wang, and Benjamin M. Comer defined the overall goal of the project and provided scientific insight and solutions. Lars Grabow defined the DFT aspect of the work. Jiefu Chen and Xuqing Wu defined machine learning aspect of the work. Ligang Lu established the Shell IP that initiated and funded the project and recruited Shell Subject Matter Experts to the project. Ligang Lu, Stefan J. Raaijman, Nishant K. Sinha, Sajanikumari Sadasiyan, Shibin Thundiyil, Kuldeep B. Mamtani, and Ganesh Iyer defined the industrial benchmarks and goals of the project. All authors contributed to and commented on the manuscript.

Conflicts of interest

This project is supported by Shell US.

Acknowledgements

The authors gratefully acknowledge financial support from Shell US. This research was performed using computational resources from the Carya, Opuntia, and Sabine clusters provided by the Research Computing Data Core at the University of Houston.

Data Availability

The entire database including the initial and relaxed structures and total energies can be accessed through the University of Houston Dataverse Repository.⁴² Details regarding the database metadata are given in the Supplementary Information.

References

- (1) Jamesh, M. I.; Sun, X. Recent progress on earth abundant electrocatalysts for oxygen evolution reaction (OER) in alkaline medium to achieve efficient water splitting – A review. *Journal of Power Sources* **2018**, *400*, 31–68.
- (2) Yuan, N.; Jiang, Q.; Li, J.; Tang, J. A review on non-noble metal based electrocatalysis for the oxygen evolution reaction. *Arabian Journal of Chemistry* **2020**, *13*, 4294–4309.
- (3) Kim, J. S.; Kim, B.; Kim, H.; Kang, K. Recent Progress on Multimetal Oxide Catalysts for the Oxygen Evolution Reaction. *Advanced Energy Materials* **2018**, *8*, 1–26.
- (4) Suen, N. T.; Hung, S. F.; Quan, Q.; Zhang, N.; Xu, Y. J.; Chen, H. M. Electrocatalysis for the oxygen evolution reaction: Recent development and future perspectives. *Chemical Society Reviews* **2017**, *46*, 337–365.
- (5) Lee, Y.; Suntivich, J.; May, K. J.; Perry, E. E.; Shao-Horn, Y. Synthesis and activities of rutile IrO₂ and RuO₂ nanoparticles for oxygen evolution in acid and alkaline solutions. *Journal of Physical Chemistry Letters* **2012**, *3*, 399–404.
- (6) Wang, Z.; Zheng, Y. R.; Chorkendorff, I.; Nørskov, J. K. Acid-Stable Oxides for Oxygen Electrocatalysis. *ACS Energy Letters* **2020**, *5*, 2905–2908.
- (7) Gunasooriya, G. T. K.; Nørskov, J. K. Analysis of Acid-Stable and Active Oxides

- for the Oxygen Evolution Reaction. *ACS Energy Letters* **2020**, *5*, 3778–3787.
- (8) Abed, J.; Heras-Domingo, J.; Luo, M.; Sanspeur, R.; Alnoush, W.; Meira, D.; Wang, H.-T.; Wang, J.; Zhou, J.; Zhou, D.; others Multi-Descriptor Design of Ruthenium Catalysts for Durable Acidic Water Oxidation. *Preprint* **2023**,
- (9) Fu, J.; Jiang, X.; Han, W.; Cao, Z. Enhancing the Cycling Stability of Transition-Metal-Oxide-Based Electrochemical Electrode via Pourbaix Diagram Engineering. *Energy Storage Materials* **2021**, *42*, 252–258.
- (10) Kang, S.; Mo, Y.; Ong, S. P.; Ceder, G. Nanoscale stabilization of sodium oxides: Implications for Na-O₂ batteries. *Nano Letters* **2014**, *14*, 1016–1020.
- (11) Sun, W. Theoretical Advancements towards Understanding Crystalline Metastability during Materials Synthesis. Ph.D. thesis, Massachusetts Institute of Technology, 2016.
- (12) Navrotsky, A. Nanoscale effects on thermodynamics and phase equilibria in oxide systems. *ChemPhysChem* **2011**, *12*, 2207–2215.
- (13) Li, Z.; Achenie, L. E.; Xin, H. An Adaptive Machine Learning Strategy for Accelerating Discovery of Perovskite Electrocatalysts. *ACS Catalysis* **2020**, *10*, 4377–4384.
- (14) Rao, K. K.; Do, Q. K.; Pham, K.; Maiti, D.; Grabow, L. C. Extendable Machine Learning Model for the Stability of Single Atom Alloys. *Topics in Catalysis* **2020**, *63*, 728–741.
- (15) Abdelfatah, K.; Yang, W.; Vijay Solomon, R.; Rajbanshi, B.; Chowdhury, A.; Zare, M.; Kundu, S. K.; Yonge, A.; Heyden, A.; Terejanu, G. Prediction of Transition-State Energies of Hydrodeoxygenation Reactions on Transition-Metal Surfaces Based on Machine Learning. *Journal of Physical Chemistry C* **2019**, *123*, 29804–29810.
- (16) Malek, A.; Wang, Q.; Baumann, S.; Guillon, O.; Eikerling, M.; Malek, K. A Data-Driven Framework for the Accelerated Discovery of CO₂ Reduction Electrocatalysts. *Frontiers in Energy Research* **2021**, *9*, 1–15.
- (17) Back, S.; Yoon, J.; Tian, N.; Zhong, W.; Tran, K.; Ulissi, Z. W. Convolutional Neural Network of Atomic Surface Structures to Predict Binding Energies for High-Throughput Screening of Catalysts. *Journal of Physical Chemistry Letters* **2019**, *10*, 4401–4408.
- (18) Chanussot, L. et al. Open Catalyst 2020 (OC20) Dataset and Community Challenges. *ACS Catalysis* **2021**, *11*, 6059–6072.
- (19) Tran, R.; Wang, D.; Kingsbury, R.; Palizhati, A.; Persson, K. A.; Jain, A.; Ulissi, Z. W. Screening of bimetallic electrocatalysts for water purification with machine learning. *The Journal of Chemical Physics* **2022**, *157*, 074102.
- (20) Price, C. C.; Singh, A.; Frey, N. C.; Shenoy, V. B. Efficient catalyst screening using graph neural networks to predict strain effects on adsorption energy. *Science Advances* **2022**, *8*.
- (21) Tran, R. et al. The Open Catalyst 2022 (OC22) Dataset and Challenges for Oxide Electrocatalysts. *ACS Catalysis* **2022**, *13*, 3066–3084.
- (22) Ong, S. P.; Richards, W. D.; Jain, A.; Hautier, G.; Kocher, M.; Cholia, S.; Gunter, D.; Chevrier, V. L.; Persson, K. A.; Ceder, G. Python Materials Genomics (pymatgen): A robust, open-source python library for materials analysis. *Computational Materials Science* **2013**, *68*, 314–319.
- (23) Persson, K. a.; Waldwick, B.; Lazic, P.; Ceder, G. Prediction of solid-aqueous

- equilibria: Scheme to combine first-principles calculations of solids with experimental aqueous states. *Physical Review B - Condensed Matter and Materials Physics* **2012**, *85*, 1–12.
- (24) Singh, A. K.; Zhou, L.; Shinde, A.; Suram, S. K.; Montoya, J. H.; Winston, D.; Gregoire, J. M.; Persson, K. A. Electrochemical Stability of Metastable Materials. *Chemistry of Materials* **2017**, *29*, 10159–10167.
- (25) Patel, A. M.; Nørskov, J. K.; Persson, K. A.; Montoya, J. H. Efficient Pourbaix diagrams of many-element compounds. *Physical Chemistry Chemical Physics* **2019**, *21*, 25323–25327.
- (26) Hjorth Larsen, A. et al. The atomic simulation environment - A Python library for working with atoms. *Journal of Physics Condensed Matter* **2017**, *29*, 1–30.
- (27) Jain, A.; Ong, S. P.; Hautier, G.; Chen, W.; Richards, W. D.; Dacek, S.; Cholia, S.; Gunter, D.; Skinner, D.; Ceder, G.; Persson, K. A. Commentary: The materials project: A materials genome approach to accelerating materials innovation. *APL Materials* **2013**, *1*, 011002 1.
- (28) Sun, W.; Ceder, G. Efficient creation and convergence of surface slabs. *Surface Science* **2013**, *617*, 53–59.
- (29) Montoya, J. H.; Persson, K. A. A high-throughput framework for determining adsorption energies on solid surfaces. *npj Computational Materials* **2017**, *3*, 14.
- (30) Kresse, G.; Hafner, J. Ab initio molecular dynamics for liquid metals. *Physical Review B* **1993**, *47*, 558–561.
- (31) Kresse, G.; Hafner, J. Ab initio molecular-dynamics simulation of the liquid-metalamorphous-semiconductor transition in germanium. *Physical Review B* **1994**, *49*, 14251–14269.
- (32) Kresse, G.; Furthmüller, J. Efficient iterative schemes for ab initio total-energy calculations using a plane-wave basis set. *Physical review. B, Condensed matter* **1996**, *54*, 11169–11186.
- (33) Kresse, G., Furthmuller, J. Software VASP, Vienna. *Physical Review B* **1996**, *54*, 169.
- (34) Blöchl, P. E. Projector augmented-wave method. 1994.
- (35) Perdew, J.; Burke, K.; Ernzerhof, M. Generalized Gradient Approximation Made Simple. *Physical review letters* **1996**, *77*, 3865–3868.
- (36) Jain, A.; Hautier, G.; Ong, S. P.; Moore, C. J.; Fischer, C. C.; Persson, K. A.; Ceder, G. Formation enthalpies by mixing GGA and GGA+U calculations. *Physical Review B* **2011**, *84*, 045115.
- (37) Gasteiger, J.; Sriram, A.; Günnemann, S.; Ulissi, Z. GemNet-OC : Developing Graph Neural Networks for Large and Diverse Molecular Simulation Datasets. *Transactions on Machine Learning Research* **2022**, 1–22.
- (38) Peterson, A. A. Global optimization of adsorbate-surface structures while preserving molecular identity. *Topics in Catalysis* **2014**, *57*, 40–53.
- (39) Musielewicz, J.; Wang, X.; Tian, T.; Ulissi, Z. FINETUNA: fine-tuning accelerated molecular simulations. *Machine Learning: Science and Technology* **2022**, *3*, 03LT01.
- (40) Shi, G.; Tano, T.; Tryk, D. A.; Yamaguchi, M.; Iiyama, A.; Uchida, M.; Iida, K.; Arata, C.; Watanabe, S.; Kakimoto, K. Temperature Dependence of Oxygen Evolution Reaction Activity in Alkaline Solution at Ni-Co Oxide Catalysts with Amorphous/Crystalline Surfaces. *ACS Catalysis* **2022**, *12*, 14209–14219.

- (41) Man, I. C.; Su, H.-Y.; Calle-Vallejo, F.; Hansen, H. A.; Martínez, J. I.; Inoglu, N. G.; Kitchin, J.; Jaramillo, T. F.; Nørskov, J. K.; Rossmeisl, J. Universality in Oxygen Evolution Electrocatalysis on Oxide Surfaces. *ChemCatChem* **2011**, *3*, 1159–1165.
- (42) Tran, R. Replication Data for: Rational design of oxide catalysts for OER with OC22. 2023; <https://doi.org/10.18738/T8/APJFTM>.
- (43) Jain, A.; Wang, Z.; Nørskov, J. K. Stable Two-Dimensional Materials for Oxygen Reduction and Oxygen Evolution Reactions. *ACS Energy Letters* **2019**, *4*, 1410–1411.
- (44) Aykol, M.; Dwaraknath, S. S.; Sun, W.; Persson, K. A. Thermodynamic limit for synthesis of metastable inorganic materials. *Science Advances* **2018**, *4*, 1–8.
- (45) Free Metal Price Tables and Charts. <https://www.dailymetalprice.com/>.
- (46) Precious Metals Dealer. <https://www.apmex.com/>.
- (47) Latest and Historical Metal Prices. www.metalarary.com.
- (48) Toxic Metals - Overview. <https://www.osha.gov/toxic-metals>.
- (49) Shi, Z.; Wang, X.; Ge, J.; Liu, C.; Xing, W. Fundamental understanding of the acidic oxygen evolution reaction: Mechanism study and state-of-the-art catalysts. *Nanoscale* **2020**, *12*, 13249–13275.
- (50) Xing, M.; Kong, L. B.; Liu, M. C.; Liu, L. Y.; Kang, L.; Luo, Y. C. Cobalt vanadate as highly active, stable, noble metal-free oxygen evolution electrocatalyst. *Journal of Materials Chemistry A* **2014**, *2*, 18435–18443.
- (51) Joya, K. S.; Ahmad, Z.; Joya, Y. F.; Garcia-Esparza, A. T.; De Groot, H. J. Efficient electrochemical water oxidation in neutral and near-neutral systems with a nanoscale silver-oxide catalyst. *Nanoscale* **2016**, *8*, 15033–15040.
- (52) Simondson, D.; Chatti, M.; Gardiner, J. L.; Kerr, B. V.; Hoogeveen, D. A.; Cherepanov, P. V.; Kuschnerus, I. C.; Nguyen, T. D.; Johannessen, B.; Chang, S. L.; Macfarlane, D. R.; Hocking, R. K.; Simonov, A. N. Mixed Silver-Bismuth Oxides: A Robust Oxygen Evolution Catalyst Operating at Low pH and Elevated Temperatures. *ACS Catalysis* **2022**, *12*, 12912–12926.
- (53) Huang, X.; Xie, M.; Chen, Y.; Zong, Q.; Liu, Z.; Jin, Y. Copper-silver oxide nanowires grown on an alloy electrode as an efficient electrocatalyst for water oxidation. *RSC Advances* **2015**, *5*, 26150–26156.
- (54) Yu, M.; hee Moon, G.; Castillo, R. G.; DeBeer, S.; Weidenthaler, C.; Tüysüz, H. Dual Role of Silver Moieties Coupled with Ordered Mesoporous Cobalt Oxide towards Electrocatalytic Oxygen Evolution Reaction. *Angewandte Chemie - International Edition* **2020**, *59*, 16544–16552.
- (55) Zhao, X.; Zhang, H.; Yan, Y.; Cao, J.; Li, X.; Zhou, S.; Peng, Z.; Zeng, J. Engineering the Electrical Conductivity of Lamellar Silver-Doped Cobalt(II) Selenide Nanobelts for Enhanced Oxygen Evolution. *Angewandte Chemie - International Edition* **2017**, *56*, 328–332.
- (56) Tian, L.; Zhai, X.; Wang, X.; Li, J.; Li, Z. Advances in manganese-based oxides for oxygen evolution reaction. *Journal of Materials Chemistry A* **2020**, *8*, 14400–14414.
- (57) Teng, Y.; Wang, X. D.; Liao, J. F.; Li, W. G.; Chen, H. Y.; Dong, Y. J.; Kuang, D. B. Atomically Thin Defect-Rich Fe–Mn–O Hybrid Nanosheets as High Efficient Electrocatalyst for Water Oxidation. *Advanced Functional Materials* **2018**, *28*, 1–8.

- (58) Hong, J. S.; Seo, H.; Lee, Y. H.; Cho, K. H.; Ko, C.; Park, S.; Nam, K. T. Nickel-Doping Effect on Mn₃O₄ Nanoparticles for Electrochemical Water Oxidation under Neutral Condition. *Small Methods* **2020**, *4*, 1–7.
- (59) Hu, C.; Zhang, L.; Zhao, Z. J.; Li, A.; Chang, X.; Gong, J. Synergism of Geometric Construction and Electronic Regulation: 3D Se-(NiCo)_{Sx}/(OH)_x Nanosheets for Highly Efficient Overall Water Splitting. *Advanced Materials* **2018**, *30*, 1–8.
- (60) Li, L.; Zhang, Y. Q.; Liu, X. Y.; Shi, S. J.; Zhao, X. Y.; Zhang, H.; Ge, X.; Cai, G. F.; Gu, C. D.; Wang, X. L.; Tu, J. P. One-dimension MnCo₂O₄ nanowire arrays for electrochemical energy storage. *Electrochimica Acta* **2014**, *116*, 467–474.
- (61) Quan, Z.; Wang, Y.; Fang, J. High-index faceted noble metal nanocrystals. *Accounts of Chemical Research* **2013**, *46*, 191–202.
- (62) Ryu, J.; Surendranath, Y. Polarization-Induced Local pH Swing Promotes Pd-Catalyzed CO₂ Hydrogenation. *Journal of the American Chemical Society* **2020**, *142*, 13384–13390.

Supplementary Information

Surface energy

To the surface energy of all bare slabs, we begin with the surface grand potential given by:

$$\gamma = \frac{E_{slab} - \sum_i n_i \mu_i}{2A} \quad (10)$$

where E_{slab} is the total energy of the bare slab, n_i is the number of atom i in the slab, μ_i is the chemical potential of atom i , A is the surface area and the factor of $\frac{1}{2}$ accounts for the two surfaces in the slab. We can define the chemical potential of each element as:

$$\mu_{A_x B_y O_z} = E_{bulk}^{A_x B_y O_z} = x\mu_A + y\mu_B + z\mu_O \quad (11)$$

where $E_{bulk}^{A_x B_y O_z}$ is the total energy per formula unit of the bulk crystal. As such, the surface energy for stoichiometric slabs can be rewritten as:

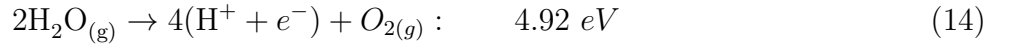
$$\gamma = \frac{E_{slab}^{A_{nx} B_{ny} O_{nz}} - nE_{bulk}^{A_x B_y O_z}}{2A} \quad (12)$$

where n is the number of bulk formula units in the slab.

We reiterate that we enumerated through all terminations per facet by modelling slabs with symmetrically equivalent terminations on each side. Inevitably, this will require the removal or addition of cations and oxygen which will lead to non-stoichiometric (relative to the bulk) slab models. In such cases, we need to compensate for the excess or deficient components by introducing variable chemical potentials per component. For any slab, there can be up to $n-1$ excess or deficient components relative to the bulk. As an example, the surface energy of a slab of $A_{nx} B_{ny+k} O_{nz-j}$ constructed from a bulk crystal of $A_x B_y O_z$ becomes:

$$\gamma = \frac{E_{slab}^{A_{nx} B_{ny+k} O_{nz-j}} - (nE_{bulk}^{A_x B_y O_z} + k\mu_B - j\frac{1}{2}\mu_{O_2})}{2A} \quad (13)$$

The chemical potential of oxygen (μ_O) can be referenced to the electrochemical decomposition of water to $O_{2(g)}$:



given by:

$$\mu_{O_2} = 4.92 + 2G_{H_2O} - 4(\mu_{H^+} + \mu_{e^-}) + \Delta G_{corr}^{O^*} \quad (15)$$

where

$$G = E + ZPE - TS^o \quad (16)$$

We can relate the proton-electron pair ($H^+ + e^-$) to the activity of the proton and the standard hydrogen electrode (SHE) using the Nernst Equation:

$$\mu_{H^+} + \mu_{e^-} = \frac{1}{2}G_{H_2} - eU + k_B T \ln a_{H^+} \quad (17)$$

Here a_{H^+} is the activity of a proton with $-pH \ln 10 = \ln a_{H^+}$ and eU is the change in electron energy under an applied potential. An excess or deficient oxygen component in the slab can be treated as an adsorbed or desorbed species and to account for this, we included a correction term, $\Delta G_{corr}^{O^*}$, to derive the Gibbs free energy of adsorption from the DFT electronic O^* adsorption energy (see Tran

et al.²¹ and Gunasooriya and Nørskov⁷ for details in regards to corrections made for the Gibbs free energy). Consequently, μ_{O_2} can be rewritten as a function of pH and U as such:

$$\mu_{O_2} = 4.92 + 2\mu_{H_2O} - 4\left(\frac{1}{2}\mu_{H_2} - eU + k_B T \ln a_{H^+}\right) + \Delta G_{corr}^{O*} \quad (18)$$

It is typical to reference the chemical potential of B (μ_B) with respect to the per atom energy of the ground state bulk crystal of pure component B (e.g. $\mu_{Fe} = \Delta\mu_{Fe} + E_{BCC,Fe}^{DFT}$). However, this is predicated upon the assumption that $A_x B_y O_z$ will immediately decompose into pure solid BCC Fe at the surface. However, multicomponent systems generally do not immediately decompose into individual solid components of each element. Herein, we assume that an excess or deficiency of components B or O at the surface will lead to slight surface passivation with a decomposition of $A_x B_y O_z$ into a more stable multicomponent guided by the phase diagram, e.g.:



In such a case, it makes sense to reference μ_B with respect to the energy of $B_y O_z$:

$$\mu_{B_y O_z} = E_{bulk}^{B_y O_z} = y\mu_B + z\mu_O \quad (20)$$

Here, the chemical potential of B increases (or decreases) with the component of B at the surface, leading to a slight passivation of $A_x B_y O_z$ to $B_y O_z$ at the surface. We can thereby rewrite μ_B as a function of μ_O

$$\mu_B = \frac{E_{bulk}^{B_y O_z} - z\mu_O}{y} \quad (21)$$

which can be substituted into Equation 13 in order to define surface energy purely as a function of μ_O and by extension U and pH in accordance with Equation 18.

Nanoparticle formation energy

The nanoparticle formation energy (G_f^{NP}) is given by Equation 4 in the main manuscript. For a material in the bulk regime ($r > 100$ nm), we can assume that the thermodynamic contributions of the surface are negligible when compared to the contribution from the bulk. However, as the particle size continues to decrease, the surface-area-to-volume ratio will increase, resulting the properties of the surface dictating the properties of the overall material. Unlike the bulk formation energy ($E_V(pH, V, T)(\frac{4}{3}\pi r^3)$), G_f^{NP} accounts for this by incorporating the surface energy contributions into the overall formation energy.

Here, $\frac{4}{3}\pi r^3$ is the volume of a nanoparticle at radius r and E_V is the Pourbaix formation energy at a given pH, U, and T per unit cell volume (E_{PBX}/V) where E_{PBX} can be derived from the following:²³⁻²⁵

$$E_{PBX} = E_0 + k_B T \ln(10)pH - n_O \mu_{H_2O}^o + (n_H - 2n_O)pH + n_{e^-}(-n_H + 2n_O + eU) \quad (22)$$

where n are the number of species in the system respectively and E_0 is the formation energy of the bulk with respect to $H_{2(g)}$ and $O_{2(g)}$:

$$E_0 = E_f + k_B T \ln(10)pH - n_{H_2O} \mu_{H_2O}^o \quad (23)$$

The contribution of the surface energy is given by $\bar{\gamma}(4\pi r^2)$ where $4\pi r^2$ is the surface area of the nanoparticle at radius r and $\bar{\gamma}$ is the surface energy of the nanoparticle. In this study, the

equilibrium crystal structure, or Wulff shape, serves as an analogue to the nanoparticle. The Wulff shape is derived through the Wulff construction whereby a set of Miller index (hkl) planes perpendicular to a vector from an origin at a distance proportional to γ_{hkl} (see Equation 1 in the main manuscript) enclose a polyhedron. The surface energy of this polyhedron is defined by:

$$\bar{\gamma}(pH, U, T, \Delta\mu_M) = \frac{\sum_{hkl} \gamma_{hkl}(pH, U, T, \Delta\mu_M) A_{hkl}}{\sum_{hkl} A_{hkl}} = \sum_{hkl} \gamma_{hkl} f_{hkl}^A(pH, U, T, \Delta\mu_M) \quad (24)$$

where (hkl) are the facets that appear on the Wulff shape and f_{hkl}^A is the fraction of area occupied by facet (hkl) on the Wulff shape.

Incorporating the surface energy contributions of the nanoparticle can consequently lead to some materials above the Pourbaix hull becoming more thermodynamically stable than the ground state material depending on the nanoparticle size.

Overpotential

The overpotential has been demonstrated to be an excellent predictor of catalytic activity in electrocatalytic processes. The overpotential (η) describes the excess amount of applied potential required to move forward in each reaction step shown in Figure 3 relative to an ideal catalyst. The summation of each reaction energy (energetic height of each reaction step or ΔG_{rxn}) is defined as the standard reduction potential in Equation 14. The ideal catalyst equally distributes the standard reduction potential along each step to minimize the required energy needed to move the reaction in the forward direction. This required energy is the equilibrium potential of OER and is given as:

$$\frac{G_{O_2} + 2G_{H_2} - 2G_{H_2O}}{4e} / = 1.23V \quad (25)$$

As such, the theoretical overpotential for an electrocatalyst is given by:

$$\eta^{OER} = \max(\Delta G_{rxn}^1, \Delta G_{rxn}^2, \Delta G_{rxn}^3, \Delta G_{rxn}^4) / e - 1.23V \quad (26)$$

where $\max(\Delta G_{rxn}^1, \Delta G_{rxn}^2, \Delta G_{rxn}^3, \Delta G_{rxn}^4)$ is the reaction energy of the potential determining step or ΔG_{rxn}^{RDS} .

The energy of each reaction step is relative to the energy of a bare slab and two water molecules in a vacuum, all of which are initially assumed to be non-interacting. Guided by Equations i-iv (see Figure 3), we can determine the DFT electronic adsorption energy of steps i-iii with the following:

$$E_{ads}^{OH^*} = E^{OH^*} + \frac{1}{2}E_{H_2} - E_{slab} - \mu_{H_2O}^o \quad (27)$$

$$E_{ads}^{O^*} = E^{O^*} + E_{H_2} - E_{slab} - \mu_{H_2O}^o \quad (28)$$

$$E_{ads}^{OOH^*} = E^{OOH^*} + \frac{3}{2}E_{H_2} - E_{slab} - 2\mu_{H_2O}^o \quad (29)$$

where E^{X^*} is the total energy of the surface intermediate with adsorbate X and E_X is the reference energy of the adsorbate in a gas. By incorporating the vibrational frequency contributions of the adsorbate on the surface in E^{ads^*} , i.e. the zero point energy and entropy, we can derive the corresponding Gibbs adsorption energies for steps i-iv:

$$\Delta G^i = G^{OH^*} + \mu_{H^+} + \mu_{e^-} - E_{slab} - G_{H_2O} \quad (30)$$

$$\Delta G^{ii} = G^{O^*} + 2(\mu_{H^+} + \mu_{e^-}) - E_{slab} - G_{H_2O} \quad (31)$$

$$\Delta G^{iii} = G^{OOH^*} + 3(\mu_{H^+} + \mu_{e^-}) - E_{slab} - 2G_{H_2O} \quad (32)$$

$$\Delta G^{iv} = 4.92V = G_{O_2} + 4(\mu_{H^+} + \mu_{e^-}) - 2G_{H_2O} \quad (33)$$

As previously mentioned, a constant correction term (ΔG_{corr}) can also be added to Equations 27-29 to obtain ΔG :

$$\Delta G^i = E_{ads}^{OH^*} + \Delta G_{corr}^{OH^*} + \mu_{H^+} + \mu_{e^-} \quad (34)$$

$$\Delta G^{ii} = E^{O^*} + \Delta G_{corr}^{O^*} + 2(\mu_{H^+} + \mu_{e^-}) \quad (35)$$

$$\Delta G^{iii} = E^{OOH^*} + \Delta G_{corr}^{OOH^*} + 3(\mu_{H^+} + \mu_{e^-}) \quad (36)$$

where $G_{corr}^{OH^*}$, $G_{corr}^{O^*}$, and $G_{corr}^{OOH^*}$ were derived in the Supplementary Information of OC22.²¹ Alternatively, if E^{OOH^*} is unavailable, well known scaling relationships between ΔG^{iii} and ΔG^i can be used instead (Figure S8)):

$$\Delta G^{iii} = \Delta G^i + 2.55 \quad (37)$$

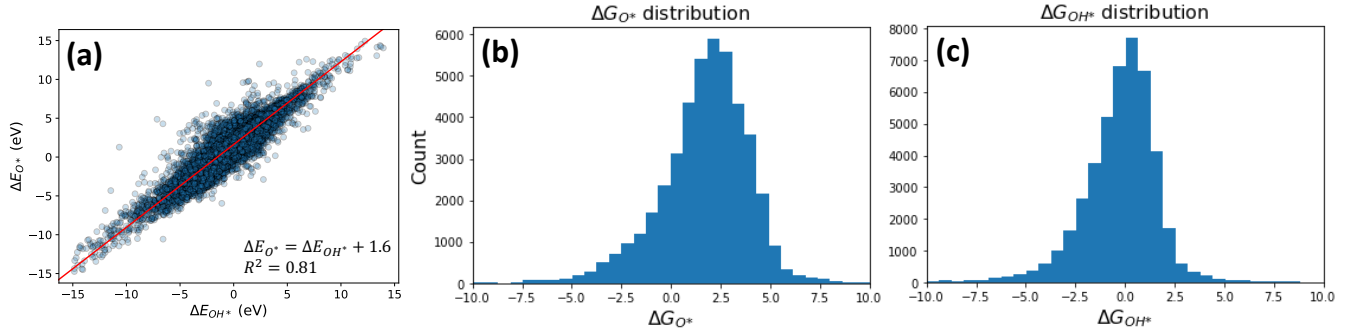


Figure 8: (a) Scaling relationship between ΔG_{OH^*} and ΔG_{O^*} . Binding energies of $\Delta G > 15eV$ or $\Delta G < -15eV$ were omitted from scaling relationship as anomalies. Distribution of adsorption energies for ΔG_{O^*} (b) and ΔG_{OH^*} (c).

From Equations 30-33 we can then obtain the individual reaction energies list in Figure 1:

$$\Delta G_{rxn}^1 = G^i \quad (38)$$

$$\Delta G_{rxn}^2 = G^{ii} - G^i \quad (39)$$

$$\Delta G_{rxn}^3 = G^{iii} - G^{ii} \quad (40)$$

$$\Delta G_{rxn}^4 = 4.92 - G^{iii} \quad (41)$$

Database usage

The entire database including the initial and relaxed structures and total energies are freely available through the University of Houston Dataverse Repository.⁴² The database comes in 3,989 [.pkl files](#) (one for each material assessed) with the mpid name followed by the '.pkl' suffix (e.g. mp-766222.pkl). Each file can be accessed by loading it with the python '[pickle](#)' module. Doing so will yield a [list](#) of python [dictionary](#) objects. Each dictionary contains the metadata and predicted information of a specific surface and all the surface intermediates (O^* , OH^* , and OOH^*) of that surface and is structured as shown in Figure S9:

Metadata of each surface includes the Materials Project ID ([entry_id](#)), the database from which the bulk structure used to generate the slab was obtained from ([database](#)), the chemical for-


```

entry_id: "mp-753534"
database: "MP"
bulk_reduced_formula: "HfCoO3"
slab_rid: "slab-o4uIeH1f5wcT1qFKuMnq"
▶ miller_index: [...]
bulk_formula: "Hf4 Co4 O12"
▶ bulk_composition: [...]
bulk_chemsys: "Co-Hf-O"
bulk_energy: -185.38058648
func: "GemNet-OC"
▼ slabs:
▶ adslab-NznP0zQDSzolCVz17Erq: [...]
▶ adslab-RrVAjRly8w65ZXWcx7JC: [...]
▶ adslab-wJLoAyA5w1ar3fMeZyKz: [...]
▶ adslab-6Jyu5uW3LUwbWX08k6bA: [...]
▶ adslab-0b6QY9AcpEfjJRYmVCI8: [...]
▶ adslab-IMLYD6Bc7cGGzx34S0aD: [...]
▶ adslab-MSJLD08Pmgz0QVfkbIkI: [...]
▶ adslab-MU2XsNGMZJGUaj7dDW68: [...]
▶ adslab-JdB0pXF2U99Zx0ELIiTM: [...]
▶ adslab-DkFLZOKVZlwIITmWRMn2: [...]
▶ adslab-jIsF6yGMVpKFPTtyMed6: [...]
▶ adslab-SdKZ7C1Rzq42u2LL3XfH: [...]
▶ adslab-6ipaQtINm7d4tApHmkCF: [...]
▶ adslab-LstM3uGvILBNYDQi6oqs: [...]
▶ adslab-sAUny9KnXI2S8nWu3HTY: [...]
▶ adslab-nsjhcFKyoZDeD6wNIA0t: [...]
▶ adslab_0maA4WtMUGUEuQXZ6osj: [...]
▶ adslab-7T5FdeuwI8ms0gJNyztU: [...]
▶ adslab-Ri4630wvqteG18JX4DC2: [...]
▼ adslab-4JMwSCzaanLlLzGv39Vh:
▶ adslab-PBhT98wCNWOACr0SbZoY: [...]
▶ adslab-z1rDw5IBFdLoLb0LPrV9: [...]
▼ slab-o4uIeH1f5wcT1qFKuMnq:

```

```

▶ cell: [...]
▶ atomic_numbers: [...]
natoms: 121
▶ tags: [...]
▶ fixed: [...]
slab_formula: "HCo24Hf22074"
entry_id: "mp-753534"
database: "MP"
adsorbate: "O0H"
slab_rid: "slab-o4uIeH1f5wcT1qFKuMnq"
rid: "adslab-4JMwSCzaanLlLzGv39Vh"
▶ miller_index: [...]
bulk_reduced_formula: "HfCoO3"
bulk_formula: "Hf4 Co4 O12"
▶ bulk_composition: [...]
bulk_chemsys: "Co-Hf-O"
bulk_energy: -185.38058648
calc_type: "adsorbed_slab"
func: "GemNet-OC"
nads: 1
y: -972.009194423662
unrelax_energy: -966.3862915039062
▶ pos_relaxed: [...]
max_force: 0.03795161843299866
▶ site_properties: [...]
▶ pmg_init_slab_fcoords: [...]

```

```

▶ cell: [...]
▶ atomic_numbers: [...]
natoms: 118
▶ tags: [...]
▶ fixed: [...]
slab_formula: "Co24Hf22072"
entry_id: "mp-753534"
database: "MP"
rid: "slab-o4uIeH1f5wcT1qFKuMnq"
▶ miller_index: [...]
bulk_reduced_formula: "HfCoO3"
bulk_formula: "Hf4 Co4 O12"
▶ bulk_composition: [...]
bulk_chemsys: "Co-Hf-O"
bulk_energy: -185.38058648
calc_type: "bare_slab"
func: "GemNet-OC"
y: -961.257409919474
unrelax_energy: -952.6406860351562
▶ pos_relaxed: [...]
max_force: 0.03443406894803047
▶ site_properties: [...]
▶ pmg_init_slab_fcoords: [...]

```

Figure 9: Dictionary object of a single entry in each database file.

mula of the bulk ([bulk_reduced_formula](#)), a unique 20 character random ID that is assigned to all slabs considered ([slab_rid](#)) with the 'slab-' prefix indicating a bare slab structure, the Miller index ([miller_index](#)), the formula of the conventional unit cell ([bulk_formula](#)), a *pymatgen* composition object ([bulk_composition](#)), the chemical system ([bulk_chemsys](#)), the total energy of the DFT computed conventional bulk structure ([bulk_energy](#)), the ML architecture used to perform the predictions ([func](#)), and a dictionary containing additional information pertaining to each individual adsorbed slab derived from the bare slab ([slabs](#)).

The [keys](#) of the slabs dictionary are the unique 20 character random ID corresponding to each slab (designated with the 'slab-' prefix) and adsorbed slab (designated with the 'adslab-' prefix). Each [value](#) of the dictionary represents a single prediction of a slab or adsorbed slab and contains its predicted properties and metadata properties. These properties are the lattice parameter matrix of the slab ([cell](#)), a list of atomic numbers making up the slab ([atomic_numbers](#)), the number of atoms in the slab ([natoms](#)), tags indicating subsurface, surface and adsorbate atoms ([tags](#)), the index of atoms that were fixed during relaxation ([fixed](#)), the formula of the slab ([slab_formula](#)), the random ID ([rid](#)), the type of calculation ([calc_type](#)), the final energy ([y](#)), the unrelaxed energy ([unrelax_energy](#)), the reference slab energy used for calculating adsorption energy ([ref_y](#)) the relaxed xyz positions of all atoms in Cartesian coordinates ([pos_relaxed](#)), the maximum force during the final relaxation step ([max_force](#)), site properties such as the bulk Wyckoff positions ([site_properties](#)), and the fractional xyz coordinates of the initial structure ([pmg_init_slab_fcoords](#)). For entries corresponding to the adsorbed slabs, we also provided the random ID of the corresponding bare slab to help expedite binding energy calculations ([slab_rid](#)).

Candidate materials

Table 2: Summary of screening criteria for our final set of 69 candidate catalyst materials for OER. Table of the formula, space group, number of facets exhibiting $\eta < 0.75$ V on the Wulff shape, lowest overpotential across the facets, whether this material exists in the bulk regime (see Methods section in the main manuscript), whether the chemical system of this material has been reported with $\eta < 0.75$ in the experimental literature, the Pourbaix formation energy (E_{PBX}), and energy above hull (E_{hull}).

Formula	Space group	facets	η (V)	Bulk	Exp.	E_{PBX} (eV)	E_{hull} (eV)	Cost (\$/kg)
FeSeO ₅	C2/c	2	0.58	True	False	0.00	-6.36	54.84
Cu ₂ AgO ₄	P $\bar{1}$	3	0.42	True	False	0.00	0.00	313.38
Ag ₃ O ₄	P2 ₁ /c	5	0.54	True	False	0.00	0.00	714.77
CoO ₂	I4/m	2	0.49	True	True	0.00	0.00	34.90
PbO ₂	Pbcn	3	0.41	True	False	0.01	0.01	2.41
Co(SbO ₃) ₂	P4 ₂ /mnm	2	0.66	True	False	0.01	0.00	17.18
CoO ₂	P $\bar{1}$	2	0.52	True	True	0.01	0.01	34.90
CaSeO ₄	P2 ₁ /c	2	0.49	True	False	0.03	0.00	65.09
AgO	P2 ₁ /c	5	0.51	True	False	0.04	0.04	745.41
Bi ₄ O ₇	P $\bar{1}$	3	0.45	True	False	0.04	0.00	22.67
FeCo ₉ O ₂₀	P $\bar{1}$	5	0.49	True	True	0.06	0.07	31.63
Bi ₂ Se ₃ O ₁₀	C2/c	2	0.67	True	False	0.07	0.00	56.01
TlFeO ₃	Pnma	2	0.50	True	False	0.07	0.05	3979.72
CaBi ₄ O ₉	P2/c	2	0.43	True	False	0.07	0.00	21.36
Li(CoO ₂) ₈	P $\bar{1}$	3	0.57	True	False	0.08	0.03	34.60
CoAgO ₃	R $\bar{3}$	2	0.49	True	False	0.09	0.09	444.63
AgSnO ₃	Cmmm	2	0.63	True	False	0.09	0.09	350.79
Na(CoO ₂) ₃	C2/m	2	0.48	True	False	0.10	0.00	51.61
Li(CoO ₂) ₄	P1	3	0.42	True	False	0.11	0.02	34.31
Cu ₃ O ₄	Ibam	2	0.50	True	False	0.13	0.03	7.89
CrAgO ₄	P2 ₁ /c	2	0.60	True	False	0.13	0.03	415.28
AgHgO ₂	P2 ₁ /c	2	0.48	True	False	0.14	0.03	302.98
In ₄ (SnO ₄) ₃	P $\bar{1}$	2	0.74	True	False	0.17	0.04	340.41
Cu ₃ Mo ₂ O ₉	P $\bar{1}$	2	0.52	True	False	0.18	0.03	19.31
Ag ₂ W ₂ O ₇	P $\bar{1}$	2	0.63	True	False	0.19	0.03	284.56
NiBiO ₃	Pnma	4	0.47	True	False	0.21	0.04	20.66
Ag ₂ BiO ₃	Pnna	2	0.66	True	False	0.24	0.00	401.94
Hg ₂ Mo ₂ O ₇	C2/c	2	0.52	True	False	0.24	0.00	42.27
K(CoO ₂) ₂	P2 ₁	3	0.45	True	False	0.24	0.00	205.67
In ₃ Cu ₃ O ₈	P2 ₁ /c	3	0.57	True	False	0.24	0.03	377.35
ZnCoO ₃	C2/c	2	0.47	True	True	0.25	0.06	19.81
V ₂ Se ₂ O ₁₁	C2/c	3	0.44	True	False	0.27	0.00	140.61

Table 3: Summary of screening criteria for our final set of 69 candidate catalyst materials for OER (continued). Bold candidates are stable at T= 60°C only.

Formula	Space group	facets	η (V)	Bulk	Exp.	E_{PBX} (eV)	E_{hull} (eV)	Cost (\$/kg)
CrSbO ₄	Cmmm	2	0.44	True	False	0.29	0.00	10.19
Ag ₂ GeO ₃	P2 ₁ 2 ₁ 2 ₁	2	0.53	True	False	0.29	0.00	862.25
LiCo ₅ O ₈	P4 ₃ 32	2	0.57	True	False	0.30	0.02	36.77
Zn ₂ SiO ₄	I42d	2	0.48	True	False	0.31	0.03	2.79
InCoO ₃	Pnma	2	0.68	True	False	0.32	0.07	387.34
Cd(GaO ₂) ₂	Pnma	2	0.49	True	False	0.32	0.07	305.35
CdAgO ₂	C2/m	2	0.58	True	False	0.32	0.02	367.40
CdAgO ₂	Pmma	2	0.61	True	False	0.32	0.03	367.40
Ca(FeO ₂) ₂	Pm	2	0.40	True	True	0.33	0.01	1.90
CoPbO ₃	R $\bar{3}$	2	0.41	True	False	0.34	0.03	11.78
SrBiO ₃	P2 ₁ /c	2	0.43	False	False	0.35	0.00	16.06
NaBi ₅ O ₈	P $\bar{1}$	2	0.49	True	False	0.35	0.03	27.24
Mn ₃ (CuO ₄) ₂	C2/m	3	0.57	False	False	0.36	0.03	4.61
AgBiO ₂	P2 ₁ /m	2	0.68	True	False	0.36	0.00	279.98
FeSnO ₃	P $\bar{1}$	2	0.57	True	False	0.38	0.00	18.17
BaTi ₂ O ₄	Pnma	2	0.43	True	False	0.38	0.00	4021.08
Cr(SbO ₃) ₂	Pnmm	3	0.63	True	False	0.38	0.06	10.88
LuCoO ₃	Pnma	2	0.46	True	False	0.40	0.03	4666.55
Co ₁₁ CuO ₁₆	P2/m	3	0.46	False	True	0.40	0.06	36.39
FeSnO ₃	Pnma	2	0.48	False	False	0.41	0.04	18.17
Li ₇ Co ₅ O ₁₂	C2/m	3	0.41	True	False	0.41	0.03	30.17
MnTiO ₃	Pnma	3	0.56	False	False	0.42	0.05	3991.79
Co ₂ NiO ₄	Imma	4	0.42	True	True	0.43	0.09	30.91
AgPbO ₂	C2/m	2	0.42	False	False	0.44	0.03	267.56
Ni ₉ O ₁₀	P $\bar{1}$	2	0.45	False	False	0.48	0.05	14.93
TlCuO ₂	P2 ₁ /m	5	0.50	False	False	0.50	0.02	4091.65
Rb ₂ Pb ₄ O ₇	P $\bar{1}$	2	0.66	False	False	0.55	0.00	12256.28
Li ₅ OsO ₆	C2/m	2	0.64	False	False	0.63	0.01	7624.17
Mn ₂ NiO ₄	Imma	2	0.42	False	False	0.69	0.01	6.48
TlTeO ₄	Cmmm	3	0.56	False	False	0.74	-5.50	3210.31
VZn ₂ O ₄	Imma	2	0.64	False	False	0.75	0.02	79.05
CoGeO ₄	Cmmm	3	0.58	False	False	0.82	-6.83	555.28
Co(SbO ₂) ₂	P4 ₂ /mbc	2	0.40	False	False	0.99	0.00	18.42
Co ₂ RuO ₄	Imma	3	0.45	False	False	1.06	0.10	8636.12
CrSbO ₄	Cmmm	2	0.66	False	False	1.08	-7.58	10.19
NaSb ₅ O ₈	P $\bar{1}$	2	0.50	False	False	1.09	0.00	19.53
GeRuO ₄	Cmmm	2	0.62	False	False	1.16	-7.38	10696.44

Table 4: Summary of screening criteria for candidate catalyst materials for OER without considering facet stability on the Wulff shape.

Formula	Space group	facets	η (V)	Bulk	Exp.	E_{PBX} (eV)	E_{hull} (eV)	Cost (\$/kg)
Ni(BiO ₃) ₂	P4 ₂ /mnm	2	0.40	True	False	0.00	0.00	20.88
FeSeO ₅	C2/c	2	0.58	True	False	0.00	-6.36	54.84
Cu ₂ AgO ₄	P1	3	0.42	True	False	0.00	0.00	313.38
Ag ₃ O ₄	P2 ₁ /c	7	0.41	True	False	0.00	0.00	714.77
PbO ₂	P4 ₂ /mnm	3	0.47	True	False	0.00	0.00	2.41
AgO	Cccm	2	0.51	True	False	0.00	0.00	745.41
CoO ₂	I4/m	2	0.49	True	True	0.00	0.00	34.90
AgO	C2/c	2	0.45	True	False	0.01	0.01	745.41
PbO ₂	Pbcn	5	0.41	True	False	0.01	0.01	2.41
Co(SbO ₃) ₂	P4 ₂ /mnm	2	0.66	True	False	0.01	0.00	17.18
CoO ₂	P1	2	0.52	True	True	0.01	0.01	34.90
Co(BiO ₃) ₂	P4 ₂ /mnm	2	0.47	True	False	0.02	0.02	24.34
Ge ₂ BiO ₆	C2/c	2	0.47	True	False	0.02	0.06	480.24
CaSeO ₄	P2 ₁ /c	2	0.49	True	False	0.03	0.00	65.09
AgO	P2 ₁ /c	6	0.51	True	False	0.04	0.04	745.41
Bi ₄ O ₇	P1	4	0.45	True	False	0.04	0.00	22.67
Cd(AgO ₂) ₂	I4 ₁ /amd	2	0.59	True	False	0.04	0.02	471.94
K ₂ Sb ₄ O ₁₁	C2/m	2	0.55	True	False	0.05	0.00	115.60
FeCo ₉ O ₂₀	P1	6	0.44	True	True	0.06	0.07	31.63
Bi ₂ Se ₃ O ₁₀	C2/c	2	0.67	True	False	0.07	0.00	56.01
TlFeO ₃	Pnma	2	0.50	True	False	0.07	0.05	3979.72
CaBi ₄ O ₉	P2/c	2	0.43	True	False	0.07	0.00	21.36
Li(CoO ₂) ₈	P1	3	0.57	True	False	0.08	0.03	34.60
Co ₃ BiO ₈	P4 ₃ 32	2	0.50	True	False	0.08	0.08	29.01
AgGeO ₃	Pbam	2	0.56	True	False	0.09	0.09	865.42
LiSbO ₃	Pnna	2	0.62	True	False	0.09	0.00	10.82
CoAgO ₃	R3	3	0.41	True	False	0.09	0.09	444.63
AgSnO ₃	Cmmm	2	0.63	True	False	0.09	0.09	350.79
Na(CoO ₂) ₃	C2/m	2	0.48	True	False	0.10	0.00	51.61
Tl ₂ O ₃	P3m1	2	0.41	True	False	0.11	-3.91	5370.69
Li(CoO ₂) ₄	P1	3	0.42	True	False	0.11	0.02	34.31
Cu ₃ O ₄	Ibam	2	0.50	True	False	0.13	0.03	7.89
CrAgO ₄	P2 ₁ /c	2	0.60	True	False	0.13	0.03	415.28
AgHgO ₂	P2 ₁ /c	2	0.48	True	False	0.14	0.03	302.98
In ₄ (SnO ₄) ₃	P1	2	0.74	True	False	0.17	0.04	340.41
Cu ₃ Mo ₂ O ₉	P1	2	0.52	True	False	0.18	0.03	19.31
Tl ₂ (SbO ₃) ₃	Pn3	2	0.66	True	False	0.18	0.05	2678.15
Ag ₂ W ₂ O ₇	P1	2	0.63	True	False	0.19	0.03	284.56

Table 5: Summary of screening criteria for candidate catalyst materials for OER without considering facet stability on the Wulff shape (continued).

Formula	Space group	facets	η (V)	Bulk	Exp.	E_{PBX} (eV)	E_{hull} (eV)	Cost (\$/kg)
TlCoO ₃	R $\bar{3}$	2	0.42	True	False	0.19	0.05	3950.09
Co(NiO ₂) ₄	C2/m	2	0.63	True	True	0.19	0.03	18.53
Bi ₂ (SeO ₃) ₃	P2 ₁ /c	2	0.45	True	False	0.20	0.00	57.07
LiAgO ₂	P2 ₁ /c	3	0.42	False	False	0.20	0.00	629.44
NiBiO ₃	Pnma	4	0.47	True	False	0.21	0.04	20.66
Cd ₂ GeO ₄	Pnma	2	0.59	True	False	0.23	0.00	293.62
Ag ₂ BiO ₃	Pnna	2	0.66	True	False	0.24	0.00	401.94
Hg ₂ Mo ₂ O ₇	C2/c	2	0.52	True	False	0.24	0.00	42.27
K(CoO ₂) ₂	P2 ₁	3	0.45	True	False	0.24	0.00	205.67
In ₃ Cu ₃ O ₈	P2 ₁ /c	4	0.57	True	False	0.24	0.03	377.35
ZnCoO ₃	C2/c	2	0.47	True	True	0.25	0.06	19.81
V ₂ Se ₂ O ₁₁	C2/c	4	0.44	True	False	0.27	0.00	140.61
CrSbO ₄	Cmmm	2	0.44	True	False	0.29	0.00	10.19
Cd ₂ PbO ₄	Pbam	2	0.51	True	False	0.29	0.00	2.59
Ag ₂ GeO ₃	P2 ₁ 2 ₁ 2 ₁	2	0.53	True	False	0.29	0.00	862.25
LiCo ₅ O ₈	P4 ₃ 32	2	0.57	True	False	0.30	0.02	36.77
NiAgO ₂	P $\bar{1}$	2	0.67	True	False	0.31	0.05	470.73
Zn ₂ SiO ₄	I42d	2	0.48	True	False	0.31	0.03	2.79
InCoO ₃	Pnma	2	0.68	True	False	0.32	0.07	387.34
Cd(GaO ₂) ₂	Pnma	2	0.49	True	False	0.32	0.07	305.35
CdAgO ₂	C2/m	2	0.58	True	False	0.32	0.02	367.40
CdAgO ₂	Pmma	3	0.61	True	False	0.32	0.03	367.40
Ca(FeO ₂) ₂	Pm	2	0.40	True	True	0.33	0.01	1.90
TiAg ₂ O ₃	C2/c	2	0.46	True	False	0.33	0.04	594.55
CoPbO ₃	R $\bar{3}$	3	0.41	True	False	0.34	0.03	11.78
SrBiO ₃	P2 ₁ /c	2	0.43	False	False	0.35	0.00	16.06
NaBi ₅ O ₈	P $\bar{1}$	2	0.49	True	False	0.35	0.03	27.24
Mn ₃ (CuO ₄) ₂	C2/m	3	0.57	False	False	0.36	0.03	4.61
AgBiO ₂	P2 ₁ /m	2	0.68	True	False	0.36	0.00	279.98
Tl ₂ Cr ₂ O ₇	P $\bar{1}$	2	0.43	True	False	0.37	0.05	3928.44
CuReO ₄	P $\bar{1}$	2	0.46	True	False	0.37	0.02	1690.40
FeSnO ₃	P $\bar{1}$	3	0.57	False	False	0.38	0.00	18.17
CoGeO ₃	C2/c	2	0.50	True	False	0.38	0.06	604.48
BaTl ₂ O ₄	Pnma	2	0.43	True	False	0.38	0.00	4021.08
LuCoO ₃	Pnma	2	0.46	True	False	0.40	0.03	4666.55
Co ₁₁ CuO ₁₆	P2/m	3	0.46	False	True	0.40	0.06	36.39
FeSnO ₃	Pnma	2	0.48	False	False	0.41	0.04	18.17
NaTlO ₂	I4 ₁ /amd	2	0.65	True	False	0.41	0.02	4751.26

Table 6: Summary of screening criteria for candidate catalyst materials for OER without considering facet stability on the Wulff shape (continued).

Formula	Space group	facets	η (V)	Bulk	Exp.	E_{PBX} (eV)	E_{hull} (eV)	Cost (\$/kg)
Li ₇ Co ₅ O ₁₂	C2/m	3	0.41	True	False	0.41	0.03	30.17
MnTiO ₃	Pnma	3	0.56	False	False	0.42	0.05	3991.79
Co ₂ NiO ₄	Imma	4	0.42	True	True	0.43	0.09	30.91
Li ₂ NiO ₃	C2/m	3	0.51	False	False	0.43	0.00	10.67
AgPbO ₂	C2/m	2	0.42	False	False	0.44	0.03	267.56
Cu ₂ W ₂ O ₇	P $\bar{1}$	2	0.46	False	False	0.47	0.10	23.94
Ni ₉ O ₁₀	P $\bar{1}$	2	0.45	False	False	0.48	0.05	14.93
PtPbO ₄	Cmmm	2	0.64	False	False	0.49	-6.04	14703.72
TiCuO ₂	P2 ₁ /m	5	0.50	False	False	0.50	0.02	4091.65
Rb ₂ Pb ₄ O ₇	P $\bar{1}$	2	0.66	False	False	0.55	0.00	12256.28
TiMnO ₃	R $\bar{3}$	2	0.45	False	False	0.62	0.00	5.36
Li ₅ OsO ₆	C2/m	2	0.64	False	False	0.63	0.01	7624.17
Mn ₂ NiO ₄	Imma	2	0.42	False	False	0.69	0.01	6.48
TlTeO ₄	Cmmm	4	0.56	False	False	0.74	-5.50	3210.31
VZn ₂ O ₄	Imma	2	0.64	False	False	0.75	0.02	79.05
CoGeO ₄	Cmmm	3	0.58	False	False	0.82	-6.83	555.28
Co(SbO ₂) ₂	P4 ₂ /mbc	2	0.40	False	False	0.99	0.00	18.42
Co ₂ RuO ₄	Imma	3	0.45	False	False	1.06	0.10	8636.12
CrSbO ₄	Cmmm	2	0.66	False	False	1.08	-7.58	10.19
NaSb ₅ O ₈	P $\bar{1}$	2	0.50	False	False	1.09	0.00	19.53
GeRuO ₄	Cmmm	2	0.62	False	False	1.16	-7.38	10696.44
K ₂ NiO ₂	I4/mmm	2	0.54	False	False	1.27	0.00	470.02